

Discovery of Interstellar 2-Cyanoindene (2-C₉H₇CN) in GOTHAM Observations of TMC-1

Madelyn L. Sita^{1,12}, P. Bryan Changala^{2,12}, Ci Xue³ , Andrew M. Burkhardt⁴ , Christopher N. Shingledecker⁵ , Kin Long Kelvin Lee^{2,3,6} , Ryan A. Loomis⁷ , Emmanuel Momjian⁸ , Mark A. Siebert⁹ , Divita Gupta¹⁰ , Eric Herbst^{1,9} , Anthony J. Remijan⁷ , Michael C. McCarthy² , Ilsa R. Cooke¹¹ , and Brett A. McGuire^{2,3,7} 

¹ Department of Chemistry, University of Virginia, Charlottesville, VA 22904, USA

² Center for Astrophysics | Harvard & Smithsonian, Cambridge, MA 02138, USA; brettmc@mit.edu

³ Department of Chemistry, Massachusetts Institute of Technology, Cambridge, MA 02139, USA

⁴ Department of Physics, Wellesley College, Wellesley, MA 02481, USA

⁵ Department of Physics and Astronomy, Benedictine College, Atchison, KS 66002, USA

⁶ Accelerated Computing Systems and Graphics Group, Intel Corporation, 2111 NE 25th Ave., Hillsboro, OR 97124, USA

⁷ National Radio Astronomy Observatory, Charlottesville, VA 22903, USA

⁸ National Radio Astronomy Observatory, Socorro, NM 87801, USA

⁹ Department of Astronomy, University of Virginia, Charlottesville, VA 22904, USA

¹⁰ I. Physikalisches Institut, Universität zu Köln, Zülpicher Str. 77, 50937 Köln, Germany

¹¹ Department of Chemistry, University of British Columbia, 2036 Main Mall, Vancouver, BC V6T 1Z1, Canada

Received 2022 August 14; revised 2022 September 13; accepted 2022 September 13; published 2022 October 17

Abstract

We present laboratory rotational spectroscopy of five isomers of cyanoindene (2-, 4-, 5-, 6-, and 7-cyanoindene) using a cavity Fourier transform microwave spectrometer operating between 6 and 40 GHz. Based on these measurements, we report the detection of 2-cyanoindene (1H-indene-2-carbonitrile; 2-C₉H₇CN) in GOTHAM line survey observations of the dark molecular cloud TMC-1 using the Green Bank Telescope at centimeter wavelengths. Using a combination of Markov Chain Monte Carlo, spectral stacking, and matched filtering techniques, we find evidence for the presence of this molecule at the 6.3 σ level. This provides the first direct observation of the ratio of a cyano-substituted polycyclic aromatic hydrocarbon to its pure hydrocarbon counterpart, in this case indene, in the same source. We discuss the possible formation chemistry of this species, including why we have only detected one of the isomers in TMC-1. We then examine the overall hydrocarbon:CN-substituted ratio across this and other simpler species, as well as compare to those ratios predicted by astrochemical models. We conclude that while astrochemical models are not yet sufficiently accurate to reproduce absolute abundances of these species, they do a good job at predicting the ratios of hydrocarbon:CN-substituted species, further solidifying -CN tagged species as excellent proxies for their fully symmetric counterparts.

Unified Astronomy Thesaurus concepts: Astrochemistry (75); Polycyclic aromatic hydrocarbons (1280); Spectral line lists (2082); Reaction rates (2081); Chemical abundances (224); Rotational spectroscopy (2248); Microwave spectroscopy (2251)

Supporting material: tar.gz file

1. Introduction

Polycyclic aromatic hydrocarbons (PAHs) may account for up to a quarter of the total carbon mass of the interstellar medium (Tielens 2008). Despite their apparent ubiquity, the formation and evolution of PAHs remain poorly constrained, highlighting the need for sensitive, targeted observations of individual PAH species in a variety of astronomical environments. Although such specificity is readily achieved by radio frequency measurements of pure rotational spectra, PAHs are notoriously difficult, if not impossible, to detect by this approach because they are often highly symmetric and therefore possess no permanent dipole moment or are at best weakly polar when not symmetric.

However, replacing even a single hydrogen on a “pure” (i.e., containing only carbon and hydrogen) PAH with a polar functional group, such as the nitrile (or cyano) unit, $\text{—C}\equiv\text{N}$, yields a spectroscopically bright surrogate. In fact, the first detections of specific interstellar PAHs were nitrile derivatives of naphthalene, 1- and 2-cyanonaphthalene (C₁₀H₇CN; McGuire et al. 2021). These discoveries were made in the dark, cold Taurus Molecular Cloud 1 (TMC-1), the same source where the simplest aromatic nitrile benzonitrile (C₆H₅CN) was first detected (McGuire et al. 2018). Taken together, and combined with complementary results from the QUIJOTE project observing TMC-1 as well (see, e.g., Cernicharo et al. 2021a), we are seeing an entirely new dimension (McCarthy & McGuire 2021) to the already rich inventory of complex organic molecules in this source (Gratier et al. 2016). Laboratory studies indicate that nitrile functionalization of benzene occurs facilely via a direct reaction of CN radicals with the aromatic double bonds, suggesting that CN tagging has the potential to be a broadly applicable scheme/strategy for quantifying otherwise radio-dark PAHs (Lee et al. 2019). Because benzene and naphthalene lack a permanent dipole moment, however, it is not possible to constrain the PAH-nitrile chemistry occurring in astronomical sources.

¹² These authors contributed equally to this work.

 Original content from this work may be used under the terms of the [Creative Commons Attribution 4.0 licence](https://creativecommons.org/licenses/by/4.0/). Any further distribution of this work must maintain attribution to the author(s) and the title of the work, journal citation and DOI.

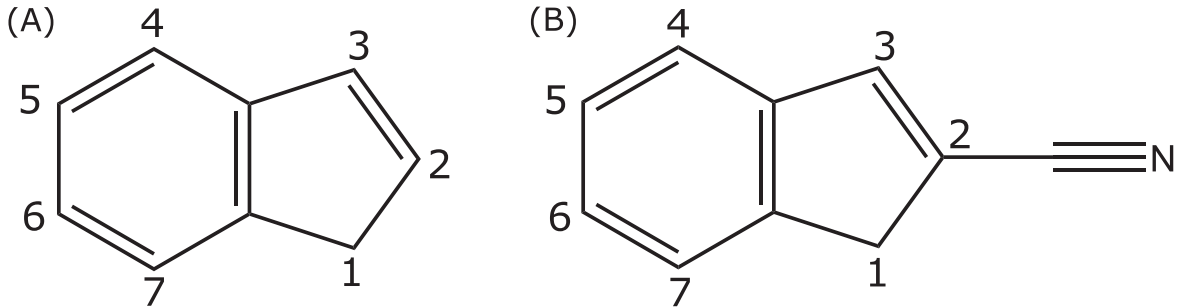


Figure 1. Chemical structure of indene (A) and 2-cyanoindene (B; $2\text{-C}_9\text{H}_7\text{CN}$). Sites 1–7 label the nitrile substitution positions of the seven possible isomers of cyanoindene.

Table 1

Parameter	1	2	3	4	5	6	7
A	2126.490335	3770.591920	2148.858711	1732.450016	3264.72881	3252.621963	1723.113358
B	971.888905	676.199976	953.096847	1145.202556	727.193886	728.881556	1155.797670
C	710.942917	575.424855	662.960551	692.411160	596.922047	597.652000	694.743761
μ_a	3.02	4.75	3.70	4.99	5.76	5.62	4.09
μ_b	2.21	0.29	3.19	2.08	1.31	0.43	1.61
μ_c	1.87
E	26.88	0.00	4.02	3.40	5.98	4.58	3.43

Note. Dipole moments have a nominal uncertainty of ± 0.5 Debye (Lee & McCarthy 2020).

The recent discovery of indene (C_9H_8 ; Figure 1) in TMC-1, the first interstellar detection of a pure PAH, now affords one an opportunity to directly link pure PAHs and their functionalized nitrile counterparts (Burkhardt et al. 2021; Cernicharo et al. 2021a), provided the latter can also be detected in the same source. To this end, this paper reports new laboratory measurements of the radio frequency transitions of five cyanoindene ($\text{C}_9\text{H}_7\text{CN}$) isomers in the 6–40 GHz spectral band. These hyperfine-resolved measurements provide the high-precision spectroscopic parameters necessary for astronomical searches of cyanoindene in cold molecular clouds. We then use these new measurements in conjunction with the latest observational data from the Green Bank Telescope Observations of TMC-1: Hunting for Aromatic Molecules (GOTHAM) survey to search for the cyanoindenes toward TMC-1. We detect the 2-cyanoindene isomer (1H-indene-2-carbonitrile; $2\text{-C}_9\text{H}_7\text{CN}$) and quantify upper limits on the column densities of four other cyanoindene isomers. We discuss these results in the context of broader astrochemical modeling of TMC-1, focusing on the ability of cyano-substituted molecules to serve as proxies of their pure hydrocarbon counterparts.

2. Laboratory Measurements

The cyanoindenes were prepared in the laboratory using similar methods to our previous experiments with benzonitrile (Lee et al. 2019) and cyanocyclopentadiene (Lee et al. 2021b; McCarthy et al. 2021). A 1 ml sample of indene, absorbed onto a cotton swab, was placed in-line behind a pulsed solenoid valve, backed with a dilute (0.1%) mixture of acetonitrile, CH_3CN , in neon at a pressure of 2.5 kTorr. The mixture was supersonically expanded along the axis of a cavity Fourier transform microwave (FTMW) spectrometer (Grabow et al. 2005) in 400 μs gas pulses at a rate of 6 Hz. During each gas pulse, a 1.2 kV discharge was struck between two copper electrodes placed immediately after the valve aperture producing reactive CN radicals, which further

reacted with indene to produce cyanoindene isomers. The molecules were efficiently cooled in the supersonic expansion to an internal rotational temperature of circa 2 K.

Using a combination of our previous indene measurements (Burkhardt et al. 2021) with theoretical structural calculations of the CN derivatives, we predicted the rotational transition frequencies of all seven possible cyanoindene isomers over the 6–40 GHz range of the cavity FTMW spectrometer. Owing to their large dipole moments (circa 5 D), transitions from several isomers were readily observed after brief searches. The rotational constants and dipole moments of each of the isomers obtained at the $\omega\text{B97X-D/6-31+G(d)}$ level of theory and basis set using the Gaussian 16 suite of programs (Frisch et al. 2016) are given in Table 1, along with relative energies obtained with the G3//B3LYP method. Ultimately, we detected five isomers with comparable abundances (2-, 4-, 5-, 6-, and 7-cyanoindene; see Figure 1 for the labeling convention), with the number corresponding to the site of the CN group. The method and basis are in line with calculations performed in our earlier GOTHAM papers, with well-characterized uncertainty in the rotational constants and dipole moments (Lee & McCarthy 2020). A .tar.gz package containing the measured laboratory frequencies, fitted spectroscopic parameters (see Table 2), electric dipole moments (Table 1), and catalog calculated from the fitted parameters for each isomer is available. The data files were generated with the SPFIT/SPCAT program suite.

The spectroscopic constants of the observed isomers were determined by least-squares fitting to an A-reduced (I') effective Hamiltonian including quartic centrifugal distortion and ^{14}N -quadrupole hyperfine parameters. These constants are summarized in Table 2. Generally, the fit quality is quite good, with residuals comparable to the 2 kHz measurement uncertainty. Some isolated centrifugal distortion constants (e.g., Δ_{JK} , Δ_K , and δ_K of isomers 5 and 6) are poorly determined but were included in the fit to treat all isomers uniformly. They have

Table 2
The Fitted Spectroscopic Constants of the Observed Cyanoindene Isomers

Parameter	2	4	5	6	7
A	3754.427(22)	1728.20692(42)	3254.849(10)	3241.0526(89)	1718.76438(50)
B	675.99176(12)	1145.625094(76)	726.94511(16)	728.82948(16)	1156.25104(11)
C	574.98249(12)	691.881285(51)	596.49419(13)	597.29716(12)	694.190200(64)
$\Delta_J \times 10^6$	5.84(22)	67.65(33)	8.31(33)	8.52(34)	71.29(86)
$\Delta_{JK} \times 10^6$	110(12)	-202.9(32)	4.4(69)	7.9(70)	-213.3(58)
$\Delta_K \times 10^3$	-18.6(73)	0.315(14)	0.14(313)	-2.0(26)	0.312(24)
$\delta_J \times 10^6$	1.42(21)	30.01(17)	1.94(21)	2.09(13)	31.71(47)
$\delta_K \times 10^3$	-0.105(58)	0.0420(27)	0.042(50)	0.005(50)	0.0403(41)
χ_{aa}	-4.223(35)	-2.0873(56)	-3.884(29)	-3.853(33)	-2.0864(56)
χ_{bb}	2.254(29)	0.1927(50)	1.941(18)	1.971(19)	0.1425(55)
N_{lines}^a	111	220	125	140	149
σ_{norm}^b	0.75	0.74	0.98	0.73	0.96
$(J, K_a)_{\text{max}}^c$	(18, 2)	(12, 6)	(16, 3)	(18, 3)	(10, 5)

Notes. The microwave transition frequencies were fitted to an A-reduced (I') effective Hamiltonian including quartic centrifugal distortion terms and ^{14}N nuclear quadrupole hyperfine structure. All dimensionful parameters are reported in MHz. Uncertainties are provided in parentheses in units of the last significant digit.

^a The number of hyperfine-resolved transitions included in the fit.

^b The rms value of the fit residuals normalized by the 2 kHz measurement uncertainty.

^c The maximum value of the J and K_a rotational quantum numbers of the states included in the fit.

little effect on the dominant a -type transitions of these isomers over this frequency range. The similarity of the rotational and hyperfine constants for the isomer pairs 4/7 and 5/6 demonstrates the near-structural equivalence of their respective substitution sites.

3. Observations

The fourth data reduction of the GOTHAM collaboration survey, hereafter referred to as DR4, includes new observations taken between 2020 June and 2022 May on the Robert C. Byrd 100 m Green Bank Telescope (GBT) in Green Bank, West Virginia. These new observations include the remainder of project code AGBT19B-047 not included in previous reductions, as well as AGBT20A-516, AGBT21A-414, and AGBT21B-210, which contributed an additional 953 hr to those presented in DR3 (Barnum et al. 2022). All previous inclusions of 19B-047 and 18B-007 were reduced again to maintain a consistent method across the new data set, while the archived data from project codes AGBT18A-333, AGBT17A-164, and AGBT17A-43 were folded in for the final spectra. DR4 extends the frequency coverage of the survey to 7.906–36.411 GHz (24.9 GHz total observed bandwidth) with a few gaps at a frequency resolution of 1.4 kHz corresponding to ~ 0.01 – 0.05 km s $^{-1}$ across the full bandwidth and improves the sensitivity (typically ~ 2 – 5 mK rms, depending on the ultimate integration time at any given frequency) and radio frequency interference (RFI) removal in areas already covered by previous reductions. This is, in part, due to a more consistent and precise method of data reduction involving a careful investigation at each observing session, scan by scan, to identify and remove RFI artifacts. The GBT beam varies from $\sim 22''$ to $95''$ over the covered frequency range.

The target, as in all GOTHAM observations, was the cyanopolyyne peak of TMC-1 at (J2000) $\alpha = 04^{\text{h}}41^{\text{m}}42\overset{\text{s}}{.}50$, $\delta = +25^{\circ}41'26''8$. All observations were conducted using position-switching mode (ON–OFF), in which the off position was 1° off target and confirmed to be clear of emission. Every ~ 2 hr, pointing and focus observations were taken using the calibrators J0530+1331 and J0359+5057, which have also

been used for flux density scale calibration. Typical pointing solutions converged to $\lesssim 5''$.

The GBT receivers are primarily calibrated by means of an internal noise diode, which we assume gives an absolute flux density calibration uncertainty of, at best, $\sim 30\%$. The noise diode in the X-band receiver was calibrated as recently as 2018 and referenced to Karl G. Jansky Very Large Array (VLA) flux density measurements (see <http://www.gb.nrao.edu/GBTCAL/>) and is therefore assumed to be better than 30%. We have taken several steps to improve the absolute flux calibration of the remaining measurements and ensure relative agreement between the two (and with X band). Initial flux density scale calibration was performed on data taken through 2020 by comparing to VLA flux density measurements obtained in 2019 and described in detail in McGuire et al. (2020). In an effort to monitor these sources for changes in flux density and cover additional frequency ranges not yet observed in the GOTHAM project as of the original calibration in 2020, VLA measurements were taken in 2021 September for both J0359+5057 and J0530+1331. Flux densities were obtained between 14 and 16 GHz (corresponding to new GOTHAM K_u -band measurements), 18.1–20.8 GHz (corresponding to new GOTHAM K -band measurements), and 34.1–36.0 GHz (corresponding to new GOTHAM Ka -band measurements). Based on a comparison to observations of these sources with the GBT, we found agreement at the 5%–10% level averaged across all observing sessions, indicating no major adjustments were needed.

As noted in McGuire et al. (2020), however, given the short-term variability of the sources, we still estimate that the uncertainty in our flux density scale calibration is at best $\sim 20\%$. We would note that each of the bands is self-consistently calibrated with an internal noise diode at the GBT. Thus, within a band, we believe that whatever the actual error in the flux density scale is (which we believe to be $\lesssim 20\%$, as discussed above), it is likely a uniform error across the entire band. Between bands, however, we suspect that the errors are nonuniform. These band-to-band variations will be more rigorously addressed with the final data reduction of the completed survey.

4. Observational Analysis

In order to derive physical parameters (column density [N_T], excitation temperature [T_{ex}], line width [ΔV], and source size [arcseconds]) for the target molecules in our observations, we used the same Markov Chain Monte Carlo (MCMC) model employed in prior GOTHAM analyses (see, e.g., Siebert et al. 2022; Lee et al. 2021c). The technique is described in detail in Loomis et al. (2021), and an exhaustive analysis of potential sources of errors, uncertainties, and spurious signals is described in the Supplementary Information for McGuire et al. (2021). In short, the MCMC model calculates probability distributions and covariances for those parameters that are used to describe the emission of molecules observed in our data. The resulting corner plots for our target species are shown in Appendix A (Figures A1 and A2). We adopt the 50th percentile value of the posterior probability distributions as the representative value of each parameter for the molecule and use the 16th and 84th percentile values for the uncertainties. For probabilities that show a Gaussian distribution, these correspond to the 1σ uncertainty level. Many of our resulting probability distributions are indeed either Gaussian or nearly Gaussian; thus, these values are usually quite representative of the 1σ uncertainties. One of the advantages of the MCMC technique over a traditional least-squares fit approach, however, is that far more parameter space is explored. Correspondingly, a much larger exploration of the uncertainty space is performed as well, including highlighting parameters that may be highly covariant with one another. This manifests as nonseparable distributions in the corner plots.

To explore this parameter space with our MCMC approach, a model of the molecular emission is generated for each set of parameters using the `molsim` software package (Lee et al. 2021a), following the conventions of Turner (1991) for a single excitation temperature, and accounting for the effect of optical depth. Prior observations from GOTHAM (Xue et al. 2020) and others (Dobashi et al. 2018, 2019) have found that most emission seen at centimeter wavelengths in TMC-1 can be separated into contributions from four distinct velocity components within the larger structure, at approximately 5.4, 5.6, 5.8, and 6.0 km s^{-1} (Loomis et al. 2021). In some cases, especially for less abundant species, where there is no clear detection in one of the velocity components, we find that a three-component model has performed better (McGuire et al. 2020).

We began first by revisiting the original detection of C_9H_8 from Burkhardt et al. (2021), which used the DR2 data from GOTHAM. Using the DR4 data, we find that a three-component model performs best with the more sensitive DR4 data, with strong detections in the 5.6, 5.8, and 6.0 km s^{-1} components. These v_{lsr} values, along with the value for T_{ex} , were used as priors for the subsequent analysis of the $\text{C}_9\text{H}_7\text{CN}$ isomers, following the same procedure.

To determine the statistical evidence that our model of the emission of these molecules is consistent with the data, we followed the procedures described in detail in Loomis et al. (2021) and performed a spectral stack and matched filtering analysis. Briefly, a weighted average of the observational spectra in velocity space and centered on each spectral line of a target molecule was performed. The weights were determined by the relative intensity of the expected emission (based on the MCMC-derived parameters) and the local rms noise of the observations. Considering the weak expected intensities for

Table 3
Summary Statistics of the Marginalized C_9H_8 Posterior

v_{lsr} (km s^{-1})	Size (arcsec)	N_T (10^{12} cm^{-2})	T_{ex} (K)	ΔV (km s^{-1})
$5.638^{+0.013}_{-0.011}$	423^{+190}_{-204}	$3.69^{+0.53}_{-0.45}$	$5.64^{+0.78}_{-0.65}$	$0.187^{+0.028}_{-0.022}$
$5.835^{+0.034}_{-0.028}$	387^{+210}_{-228}	$1.67^{+0.53}_{-0.71}$		
$6.019^{+0.015}_{-0.012}$	430^{+184}_{-204}	$3.67^{+0.60}_{-0.47}$		
$N_T(\text{Total})$:				$9.04^{+0.96}_{-0.96} \times 10^{12} \text{ cm}^{-2}$

Note. The quoted uncertainties represent the 16th and 84th percentile (1σ for a Gaussian distribution) uncertainties. Uncertainties derived by adding the uncertainties of the individual components in quadrature.

both C_9H_8 and the $\text{C}_9\text{H}_7\text{CN}$ isomers, any observational windows containing emission at $>5\sigma$ were ignored in this analysis. Given the low line density of the spectra, the number of spectral regions flagged this way is small; e.g., for indene, 1% of the data needed to be rejected in this way, while for 2-cyanoindene, only 0.6% of the data were rejected. Simulated spectra of the molecular emission using the same MCMC-derived parameters were then also generated and stacked using identical weights. This simulation was then used as a matched filter, which is passed through the observational signal. The resulting impulse response function represents the statistical evidence that our model of the emission from the molecule—and thus our derived parameters for the molecule—is consistent with the observations. In addition to the details of the methodology provided in Loomis et al. (2021), the appendices of McGuire et al. (2021) include an extensive analysis of the robustness of the methodology, including the improbability of spurious signals and the minimal impact of red noise on the procedure.

5. Results

The resulting parameters from the MCMC inference to C_9H_8 emission in the DR4 observational data are shown in Table 3; the corner plot is shown in Figure A1. The new column density derived from the DR4 data, $9.04^{+0.96}_{-0.96} \times 10^{12} \text{ cm}^{-2}$, falls firmly within the uncertainty range of our previous value, $9.60^{+4.33}_{-1.57} \times 10^{12} \text{ cm}^{-2}$ (Burkhardt et al. 2021), but has a narrower range of uncertainties reflecting the increased quality of the DR4 data. We note that the value derived for the excitation temperature, $T_{\text{ex}} = 5.64 \text{ K}$, is lower than that found previously in our DR2 data of $T_{\text{ex}} = 8.55 \text{ K}$. We and others (see, e.g., Cernicharo et al. 2021b) continue to find that excitation temperatures within TMC-1 fall between ~ 5 and 9 K . In the GOTHAM data, the values derived are extremely sensitive to the number of higher-energy transitions observable at higher frequencies, the quality of the data at those frequencies, and the relative flux calibration throughout the survey. This is further complicated by the large uncertainties in the source sizes, which differentially affect beam dilution corrections at the low ($\sim 10 \text{ GHz}$) and high ($\sim 30 \text{ GHz}$) ends of our data, where the telescope beam sizes vary significantly. Combined with the difficulties in constraining the flux uncertainty discussed above, we would caution that the quoted statistical uncertainties on the derived values of T_{ex} in the GOTHAM data are likely underestimated. The ultimate effect of the small change in T_{ex} on the other derived parameters, particularly N_T , however, is negligible.

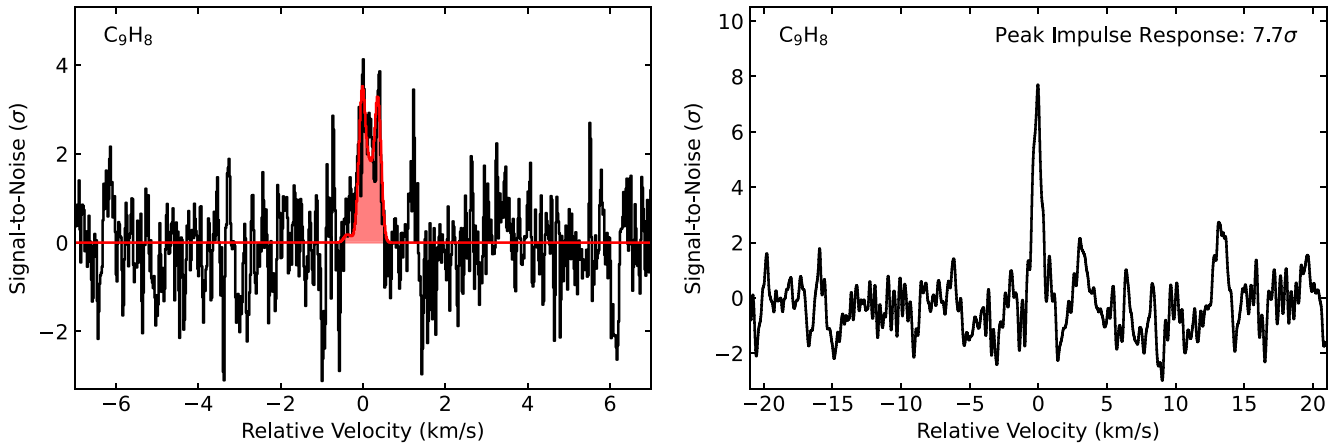


Figure 2. Velocity stacked and matched filter spectra of C_9H_8 . The intensity scales are the signal-to-noise ratios of the response functions when centered at a given velocity. The “zero” velocity corresponds to the channel with the highest intensity to account for blended spectroscopic transitions and variations in velocity component source sizes. (Left) The stacked spectra from the GOTHAM DR4 data are displayed in black, overlaid with the expected line profile in red from our MCMC fit to the data. The signal-to-noise ratio is on a per-channel basis. (Right) Matched filter response obtained from cross-correlating the simulated and observed velocity stacks in the left panel; the value annotated corresponds to the peak impulse response of the matched filter.

Using these updated parameters for our three-component model of the emission of C_9H_8 , we generated a spectral stack and performed a matched filtering analysis as described above. The results are shown in Figure 2. The evidence for a detection of indene in our data has increased from 5.7σ , as reported in Burkhardt et al. (2021), to 7.7σ , reflecting the increased spectral coverage and higher signal-to-noise ratio of the DR4 data set.

We see statistically significant evidence ($>5\sigma$) for the presence of only a single isomer of $\text{C}_9\text{H}_7\text{CN}$, isomer 2 ($2\text{-C}_9\text{H}_7\text{CN}$), which exhibits a peak impulse response of 6.3σ . The best-fit parameters from the MCMC fit for this isomer are shown in Table 4, and the spectral stack and matched filter are shown in Figure 3; the corner plot is shown in Figure A2. The MCMC analyses for the other isomers resulted in no significant signal being detected. Upper limits to the column densities for the other species are provided in Table 5.

Finally, Figure 4 shows the ratios of the column densities of several pure hydrocarbon species to their $-\text{CN}$ substituted counterparts as measured by observations in TMC-1 and predicted by the chemical models of Burkhardt et al. (2021) and Siebert et al. (2022). The measured values were obtained by taking the ratio of the reported best-fit total column densities, while the uncertainties were obtained by taking the ratio of the extremes of the errors on those individual measurements. For example, for the $\text{C}_9\text{H}_8/2\text{-C}_9\text{H}_7\text{CN}$ ratio, the reported column densities with errors are $9.04^{+0.96}_{-0.96}$ and $0.210^{+0.060}_{-0.046} \times 10^{12} \text{ cm}^{-2}$. The location of the black circle corresponds to $9.04/0.210 = 43$. The upper end of the uncertainty was obtained by taking the upper end of the $\text{C}_9\text{H}_8 N_T$ ($9.04 + 0.96 = 10.0$) and dividing by the lower end of the $2\text{-C}_9\text{H}_7\text{CN} N_T$ ($0.210 - 0.046 = 0.164$) for a final value of $10.0/0.164 = 61$.

6. Discussion

With the detections of benzonitrile ($\text{C}_6\text{H}_5\text{CN}$) and the two cyanonaphthalene species ($\text{C}_{10}\text{H}_7\text{CN}$), the cyanoindenes ($\text{C}_9\text{H}_7\text{CN}$) were appealing targets to search for. The detection of $2\text{-C}_9\text{H}_7\text{CN}$ not only expands the number of individual PAH species detected in space to four, but it offers the first

Table 4
Summary Statistics of the Marginalized $2\text{-C}_9\text{H}_7\text{CN}$ Posterior

v_{lsr} (km s $^{-1}$)	Size (arcsec)	N_T (10^{10} cm^{-2})	T_{ex} (K)	ΔV (km s $^{-1}$)
$5.492^{+0.047}_{-0.054}$	435^{+179}_{-204}	$6.85^{+2.08}_{-1.80}$	$5.09^{+0.52}_{-0.48}$	$0.247^{+0.048}_{-0.047}$
$5.899^{+0.040}_{-0.168}$	394^{+206}_{-227}	$6.04^{+3.99}_{-2.18}$		
$5.946^{+0.031}_{-0.027}$	380^{+220}_{-230}	$8.10^{+3.96}_{-3.61}$		
$N_T(\text{Total})$: $2.10^{+0.60}_{-0.46} \times 10^{11} \text{ cm}^{-2}$				

Note. The quoted uncertainties represent the 16th and 84th percentile (1σ for a Gaussian distribution) uncertainties. Uncertainties derived by adding the uncertainties of the individual components in quadrature.

opportunity for a direct observational comparison of a $-\text{CN}$ substituted PAH to its pure hydrocarbon counterpart.

Of the possible isomers of $\text{C}_9\text{H}_7\text{CN}$, we detect only $2\text{-C}_9\text{H}_7\text{CN}$. While $2\text{-C}_9\text{H}_7\text{CN}$ is the lowest-energy species (the next highest being isomers 4 and 7, roughly 3.4 kJ mol^{-1} (409 K) higher in energy; see Table 1), it is not immediately obvious that this should be the only controlling factor. The reaction pathway currently in astrochemical models for the formation of cyanoindene from C_9H_8 is by direct attack by CN radicals resulting in H-atom loss (Equation (1); see Doddipatla et al. 2021):



We note that the model does not distinguish between the possible isomeric forms of cyanoindene, however.

If the reaction between CN and indene in Doddipatla et al. (2021) is analogous to the production of benzonitrile from benzene via Equation (2),



then we would expect attack at any of the double bonds to be efficient and barrierless (Balucani et al. 1999; Cooke et al. 2020). It has been shown both experimentally and theoretically that addition–elimination reactions between CN and unsaturated hydrocarbons do not have barriers in their entrance channel and proceed via addition complexes (Carty et al. 2001; Sims et al. 1993; Woon & Herbst 1997). Indeed, that all

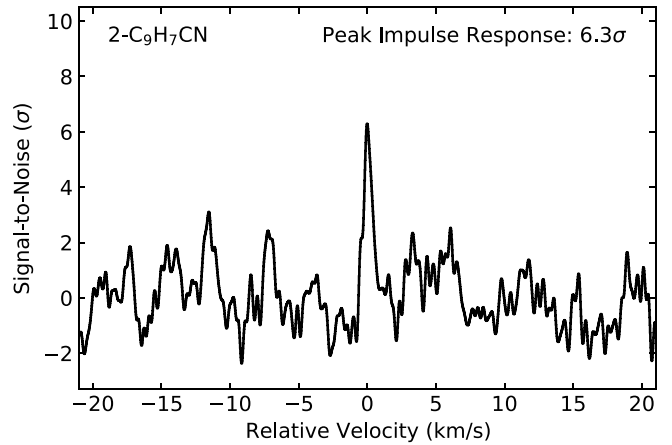
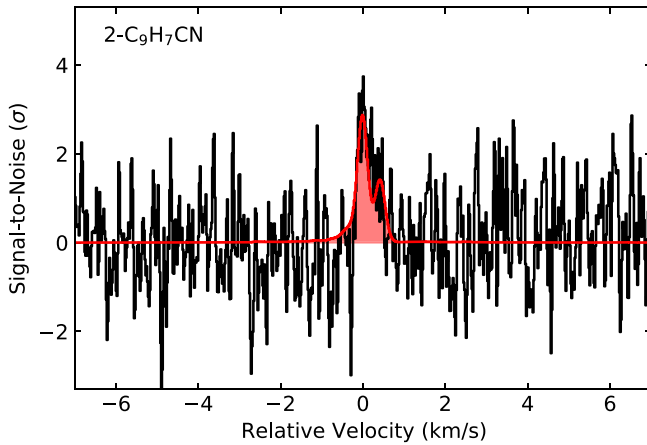
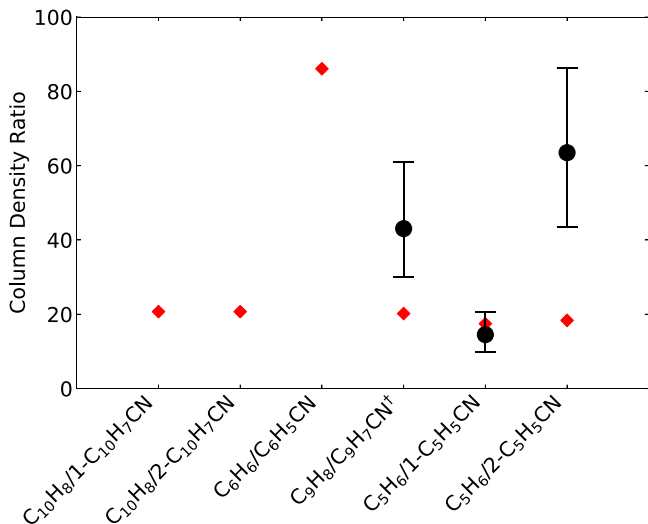
Figure 3. Same as Figure 2 but for 2-C₉H₇CN.

Figure 4. Ratios of the column density of pure hydrocarbon species to their -CN substituted counterparts as predicted by our chemical models (red diamonds; Burkhardt et al. 2021) compared to those measured by the GOTHAM and QUIJOTE surveys (black circles with error bars). Table B1 provides the values used and specific references.

^aFor C₉H₇CN, the measured value takes only 2-C₉H₇CN into account, while the model-predicted value includes all of the isomers.

isomers save 1 and 3 are detected with comparable abundance in the laboratory suggests low site specificity, albeit in a high-energy, high-density discharge source. With the exception of the *sp*³-hybridized carbon at position 1, it is not unreasonable in such an environment to assume that a nonzero branching fraction into the different isomers could occur based on the angle of approach of the CN radical relative to *sp*²-hybridized carbons in C₉H₈.

For asymmetrical unsaturated molecules like indene, however, the site of addition can often dictate the product-branching ratios. In general, the radical will attack at the least substituted position of the unsaturated bond, forming the more stable radical intermediate; however, this is not always the case, as has been observed for propene, where the position of the initial CN attack does not determine the product distribution (Huang et al. 2009). For some addition reactions, optimal orientation of the reactants for the long-range interaction results in a van der Waals potential minimum, which will influence the

Table 5
Column Density and Column Density Upper Limit Determinations for the Seven Isomers of Cyanoindene

Isomer	Total Column Density (10 ¹¹ cm ⁻²)
1	...
2	2.10 ^{+0.60} _{-0.46}
3	...
4	<1.7
5	<5.1
6	<3.3
7	<4.7

Note. Upper limits are reported as the sum of the 97.5th percentiles (3 σ for a Gaussian distribution) of the posteriors for each velocity component for a given molecule. Uncertainties on isomer 2 were derived by adding the uncertainties of the individual components in quadrature.

^a No laboratory frequencies available.

reaction kinetics and product distribution (Georgievskii & Klippenstein 2007; Cheikh Sid Ely et al. 2013).

Our current analysis cannot constrain the other isomers to be significantly less abundant than 2-cyanoindene. Were further observations to indeed show that they are less abundant, that might then suggest that there could be a degree of thermodynamic control. Whether or not all of the thermodynamically allowed products can be accessed will depend on the lifetime of the addition complex and the energy barriers to forming products. If the complex is long-lived, energy transfer within the adduct will likely result in a statistical product distribution. It is unlikely that the complex will be collisionally stabilized under TMC-1 conditions. If the lifetime is very short, the complex cannot explore all regions of phase space, and the products will be controlled by dynamics, i.e., will not be statistical in nature.

To investigate this further, we have calculated the potential energy surface for the CN addition channels in the CN + C₉H₈ reaction (see Appendix C). Comparing to similar reactions of CN with aromatic hydrocarbons, for example, CN + benzene (Woon 2006), CN + toluene (Messinger et al. 2020), and CN + styrene (Landera & Mebel 2013), we expected that the reaction would occur via CN addition to a double bond, either in the six- or five-membered ring. The addition proceeds via

radical intermediates that can decompose to products or perhaps rearrange to other isomers that can decompose to different products. Determining the product distributions will require a multiwell treatment of the interconnected minima and products.

One may also speculate whether CN addition to the double bond in the five-membered ring is favored in these types of systems. Considering that the additions to each of these sites are barrierless and rapid, the simplest assumption one can make is that they are equally likely. Our calculations show that the intermediates formed from addition to the double bonds (with the exception of the 3-position) are resonance-stabilized radicals (shown in Figures C3 and C4). The relative energies of the CN addition complexes are given in Table C2. Addition to double bonds in the aromatic six-membered ring is less favorable thermodynamically, as the radical intermediates result in loss of the aromaticity. Addition at the 2-position in the five-membered ring forms the most stable intermediate of the six possible addition complexes. Addition at this site forms a benzylic radical intermediate, which may be the reason that it is especially stable. In contrast, addition to the 3-position results in a radical intermediate that cannot be resonance-stabilized, as the radical site is now displaced from the π system of the aromatic ring. More work is required to reduce the uncertainty on the abundances of the other cyanoindene isomers. Since most of their upper limits fall above the observed column density of 2-cyanoindene, we cannot be certain that this isomer is formed preferentially in TMC-1, and more observational evidence is needed. If 2-cyanoindene is indeed the only isomer detected, this would suggest that reaction at the 2-position is kinetically favored or the initial addition complexes have efficient isomerization pathways that can reorient to form the 2-C₉H₇CN product. Grain-surface pathways might also present a mechanism for rearrangement into a thermodynamically favored interaction prior to product formation. Further quantum chemical work is needed to explore the full reaction landscape.

Regardless, we are now able to directly compare the ratio of a pure hydrocarbon PAH to its –CN substituted counterpart (hereafter HC:CN) in observations versus those predicted by our astrochemical models (Burkhardt et al. 2021). As we have described before, our models (McGuire et al. 2021; Burkhardt et al. 2021), as well as others (Cernicharo et al. 2021b), usually fail to reproduce the absolute observed abundances of PAHs and other large cyclic species, both purely hydrocarbon and –CN derivatives, by several orders of magnitude or more. As nearly all of the –CN species are formed in these models by direct attack by CN radicals, as shown in or analogous to Equations (1) and (2), we suspect the failure of the models is due to incomplete reaction networks leading to the under-production of the pure hydrocarbon species. While these networks can be improved using the results of ongoing laboratory experiments (see, e.g., Doddipatla et al. 2021) or quantum chemical calculations, many of the pure hydrocarbon species lack a permanent dipole. As a result, we have no observational constraints on their abundances with which to compare and constrain the updated networks.

One way around this problem is through the observation of the –CN derivatives, but this only serves as an effective proxy if we have at least a decent understanding of the expected HC:CN ratio. As shown in Figure 4, the HC:CN ratio predicted by astrochemical models for a range of species pairs for which at

least one of the molecules is detected in TMC-1 is relatively consistent at a value of ~ 20 . We note again that the model results presented here from Burkhardt et al. (2021) did not distinguish between cyanoindene isomers. Thus, a full comparison of the ratios of C₉H₈/C₉H₇CN shown in Figure 4 for the observation and model results would require either a reworking of the model to account for the branching into different isomers (thus increasing the modeled C₉H₈/C₉H₇CN ratio) or the adjustment of the observations to include the upper limits of the other isomers (thus lowering the observed C₉H₈/C₉H₇CN ratio). Either scenario is beyond the scope of the present work but would actually bring the two values closer into agreement than present.

Of the ratios shown in Figure 4, the outlier, the ratio of C₆H₆/C₆H₅CN, still differs only by a factor of ~ 4 from the others. This discrepancy is due to the fact that our astrochemical models use the experimentally determined value for the rate coefficient of Equation (2) of $5.4 \times 10^{-10} \text{ cm}^3 \text{ s}^{-1}$ determined at 15 K by Cooke et al. (2020), whereas the other hydrocarbon + CN reactions use the values of $(1.0\text{--}1.5) \times 10^{-10} \text{ cm}^3 \text{ s}^{-1}$ (Burkhardt et al. 2021). Our results may suggest that this rate is indeed also too low, and we suggest that these reactions would be excellent targets for follow-up experimental studies. Until then, however, we have no compelling justification to alter the rates in the models. Nevertheless, the difference in derived ratios remains, by the standards of astrochemical models and observations, quite small.

This consistency is, again, due largely to the similar formation reaction pathways and rates used to produce these species. Prior observations of the HC:CN ratio for cyclopentadiene and its two CN derivatives agree with the model predictions to within a factor of $\sim 2\text{--}5$. With the detection of 2-C₉H₇CN, we can now posit that that agreement extends to the PAHs as well, and that –CN derivative species can indeed be used as an excellent observational proxy for their hydrocarbon counterparts for constraining models, at least within a factor of a few.

7. Conclusions

We report the first interstellar detection of 2-cyanoindene, 2-C₉H₇CN, with a significance of 6.3σ in GOTHAM observations of TMC-1. Of seven potential structural isomers, only the lowest-energy form was detected with any significance. Though chemical models often underpredict the observed abundances of PAH molecules or their –CN derivatives in TMC-1, this detection shows that, even so, the calculated ratios of the abundances of the pure hydrocarbon to CN-substituted forms are likely still accurate to within a factor of $\sim 2\text{--}5$. Thus, combined with existing laboratory and computational studies, we conclude that cyano-PAHs are excellent observational proxies for their pure hydrocarbon counterparts. Further computational or experimental work is required to fully explain the detection of only a single isomer of C₉H₇CN.

We gratefully acknowledge support from NSF grants AST-1908576 and AST-2205126. I.R.C. acknowledges support from the University of British Columbia and the Natural Sciences and Engineering Research Council of Canada (NSERC). The National Radio Astronomy Observatory is a facility of the National Science Foundation operated under cooperative agreement by Associated Universities, Inc. The

Green Bank Observatory is a facility of the National Science Foundation operated under cooperative agreement by Associated Universities, Inc.

Statement of Efforts. All authors contributed to the writing and editing of the manuscript. M.L.S performed the data reduction and calibration of the DR4 data set. P.B.C. performed laboratory measurements. A.M.B. provided astrochemical modeling results. I.R.C., R.A.L., and C.X. aided in the analysis of the observational data. C.X. designed and performed the observations of project code GBT21A-414 and developed the scripts for analysis and corner plot generation. K.L.K.L. performed the quantum chemical calculations and laboratory

measurements. E.M. performed and reduced the VLA flux density calibration measurements. D.G. performed quantum chemical calculations for CN addition to rings. C.N.S., I.R.C., E.H., D.G., and P.B.C. contributed to the discussions of formation branching ratios. B.A.M. performed the analysis of the observational data and designed the project.

Appendix A MCMC Analysis Results

The corner plots resulting from the analysis of C_9H_8 and 2- $\text{C}_9\text{H}_7\text{CN}$ are shown in Figures A1 and A2, respectively.

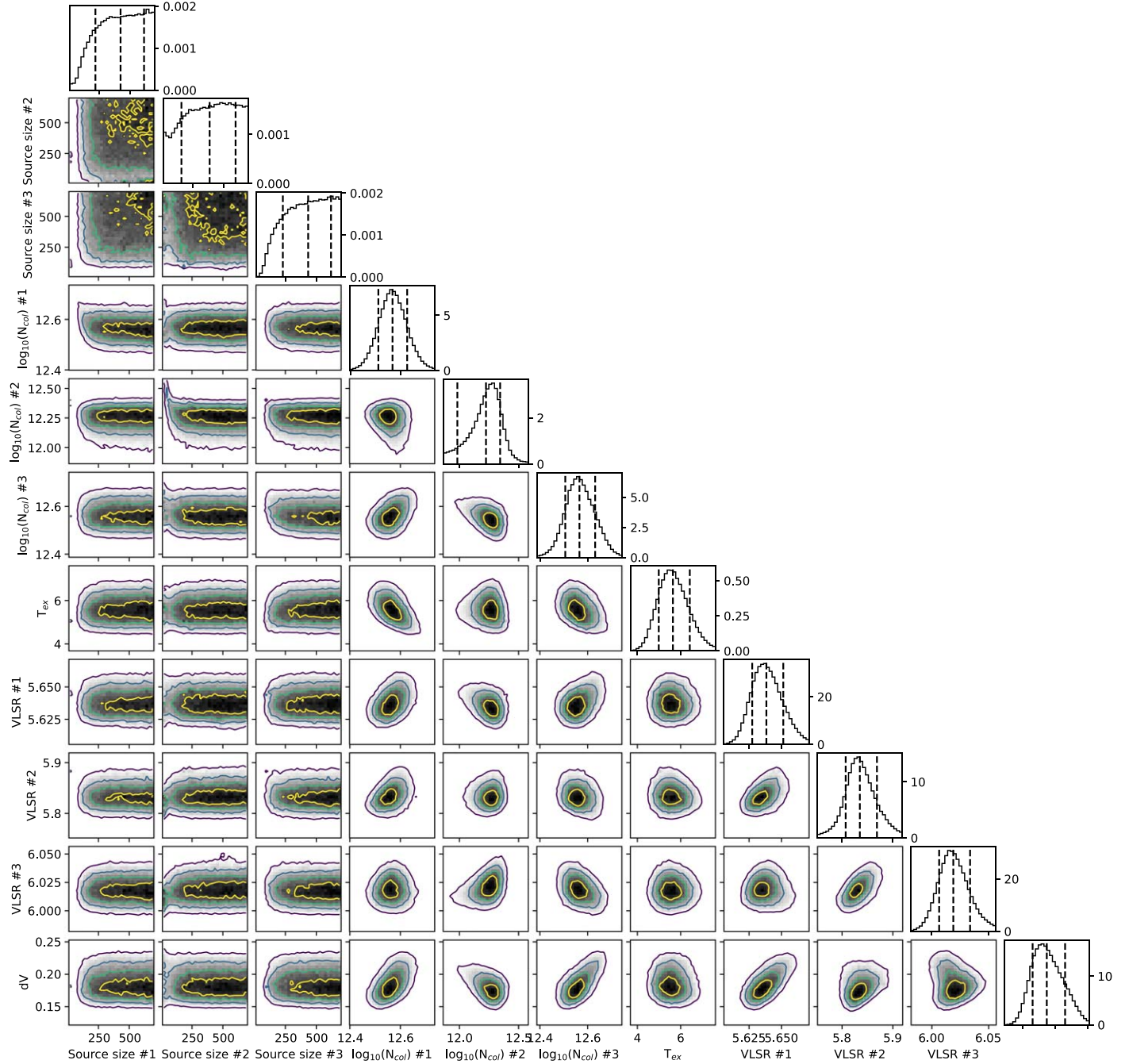


Figure A1. Corner plot for C_9H_8 showing parameter covariances and marginalized posterior distributions for the C_9H_8 MCMC fit. The 16th, 50th, and 84th confidence intervals (corresponding to $\pm 1\sigma$ for a Gaussian posterior distribution) are shown as vertical lines.

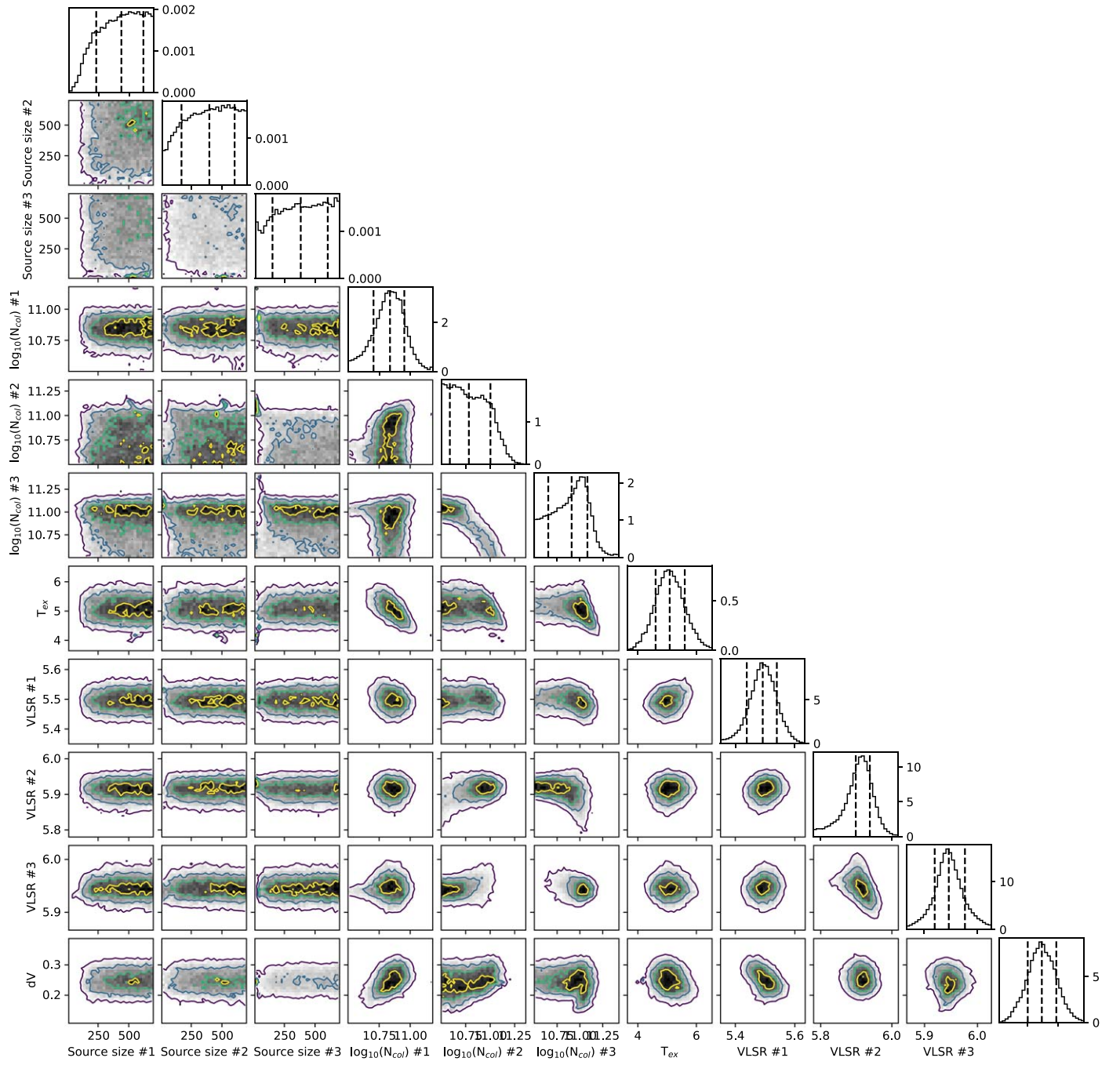


Figure A2. Corner plot for 2-C₉H₇CN showing parameter covariances and marginalized posterior distributions for the 2-C₉H₇CN MCMC fit. The 16th, 50th, and 84th confidence intervals (corresponding to $\pm 1\sigma$ for a Gaussian posterior distribution) are shown as vertical lines.

Appendix B

Observed Column Densities of Hydrocarbon Species and Their -CN Substituted Analogs

Table B1 provides the column densities of the species plotted in Figure 4 observed in TMC-1.

Table B1
Column Densities of Species Plotted in Figure 4 Observed in TMC-1

Molecule	Column Density (10^{12} cm^{-2})	Reference
C_5H_6	12^{+3}_{-3}	Cernicharo et al. (2021a)
1- $\text{C}_5\text{H}_5\text{CN}$	$0.827^{+0.09}_{-0.10}$	Lee et al. (2021b)
2- $\text{C}_5\text{H}_5\text{CN}$	$0.189^{+0.018}_{-0.015}$	Lee et al. (2021b)
C_9H_8	$9.04^{+0.96}_{-0.96}$	This work
2- $\text{C}_9\text{H}_7\text{CN}$	$0.210^{+0.060}_{-0.046}$	This work

Appendix C

Quantum Chemical Calculations for CN Addition to the Indene Ring

Table C1 lists the relative energies of the complexes formed after CN addition to the indene ring. It is noted that the complex formed by CN addition at the carbon position 2 is the most stable among the six possible addition complexes.

Figures C1 and C2 show the complete potential energy surface obtained for the CN addition channels for CN +

indene. The quantum calculations were performed using Gaussian 16 software (Frisch et al. 2016). All of the species, including the addition complexes and transition states, were optimized at the (U)B3LYP-G3/def2-TZVP level, and zero-point corrected energies were calculated for each. In addition, intrinsic reaction coordinate calculations were performed at (U) B3LYP-G3/def2-TZVP to determine the minimum energy path that the transition states followed to confirm the connection between the appropriate reactants and products.

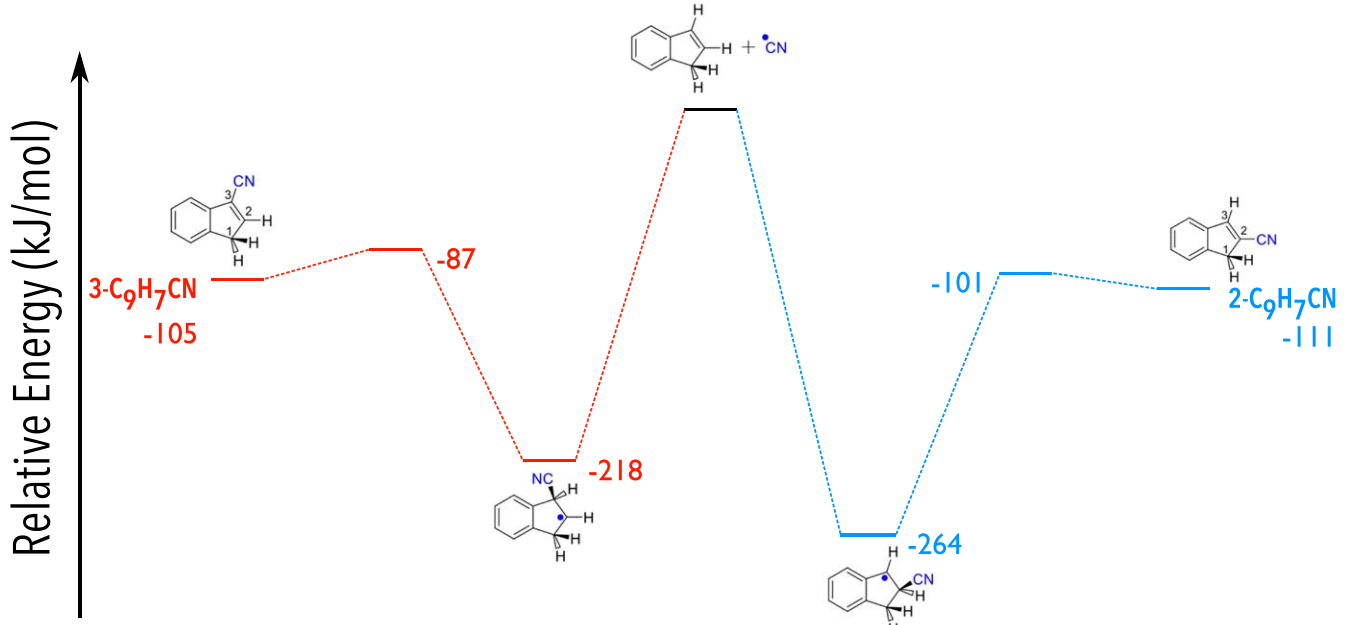


Figure C1. Potential energy surface ((U)B3LYP-G3/def2-TZVP) for the CN addition–H elimination channels for the reaction between CN and indene. Two possible channels occur via CN addition at carbon positions 2 and 3 for the five-membered ring.

Table C1
Relative Energies, Provided in kJ mol^{-1} , of the CN Addition Complexes Calculated at (U)B3LYP-D3/def2-TZVP

CN Addition Complex	Relative Energy (kJ mol^{-1})
2-C ₉ H ₈ CN	-263.7
3-C ₉ H ₈ CN	-217.9
4-C ₉ H ₈ CN	-187.5
5-C ₉ H ₈ CN	-174.0
6-C ₉ H ₈ CN	-191.9
7-C ₉ H ₈ CN	-174.9

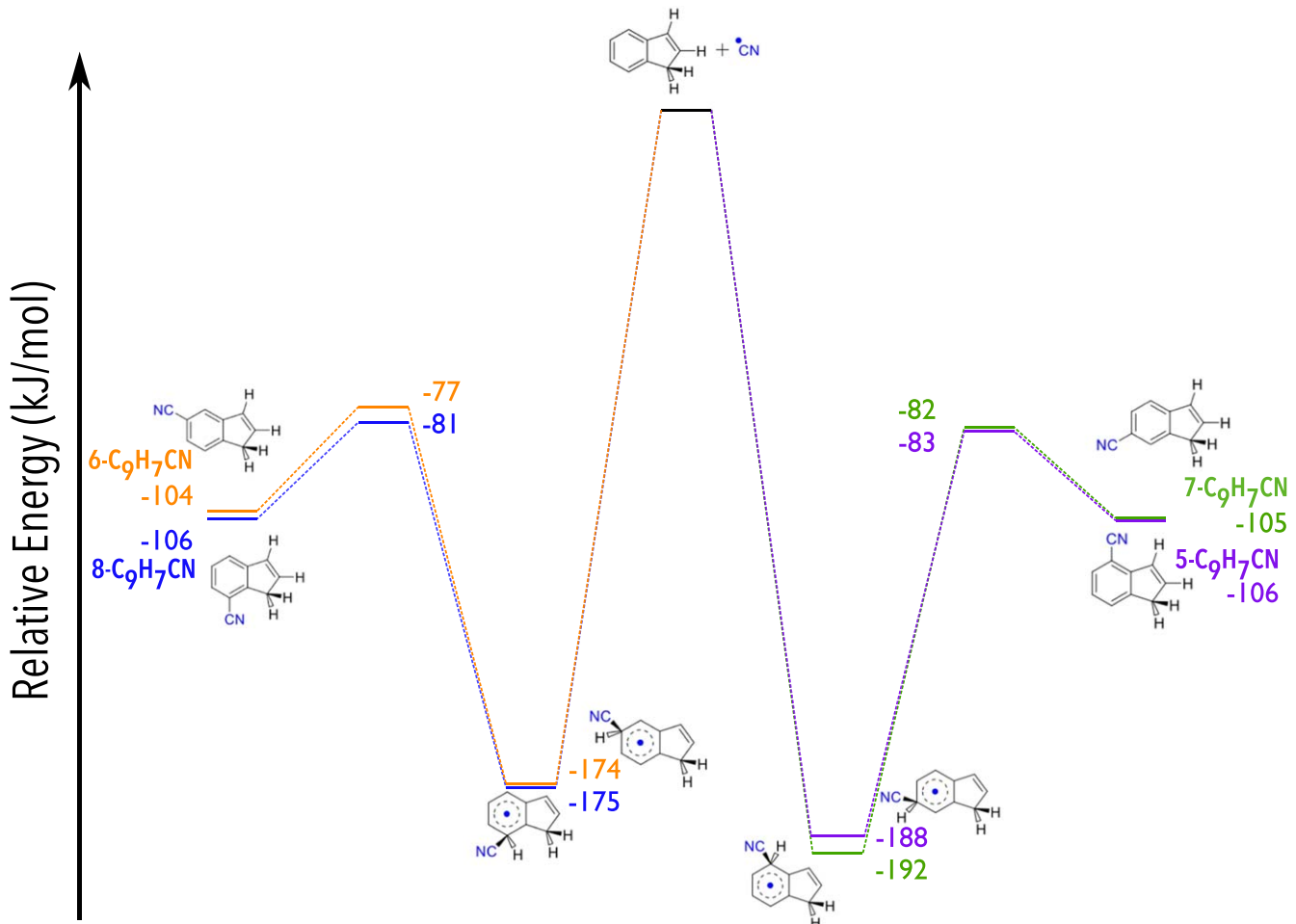


Figure C2. Potential energy surface ((U)B3LYP-G3/def2-TZVP) for the CN addition–H elimination channels for the reaction between CN and indene. Four possible channels occur via CN addition at carbon positions 5, 6, 7, and 8 for the six-membered ring.

ORCID iDs

Ci Xue <https://orcid.org/0000-0003-2760-2119>
 Andrew M. Burkhardt <https://orcid.org/0000-0003-0799-0927>
 Christopher N. Shingledecker <https://orcid.org/0000-0002-5171-7568>
 Kin Long Kelvin Lee <https://orcid.org/0000-0002-1903-9242>
 Ryan A. Loomis <https://orcid.org/0000-0002-8932-1219>
 Emmanuel Momjian <https://orcid.org/0000-0003-3168-5922>
 Mark A. Siebert <https://orcid.org/0000-0002-8505-4934>
 Eric Herbst <https://orcid.org/0000-0002-4649-2536>
 Anthony J. Remijan <https://orcid.org/0000-0001-9479-9287>
 Michael C. McCarthy <https://orcid.org/0000-0001-9142-0008>
 Ilisa R. Cooke <https://orcid.org/0000-0002-0850-7426>
 Brett A. McGuire <https://orcid.org/0000-0003-1254-4817>

References

Balucani, N., Asvany, O., Chang, A. H. H., et al. 1999, *JChPh*, **111**, 7457
 Barnum, T. J., Siebert, M. A., Lee, K. L. K., et al. 2022, *JPCA*, **126**, 2716
 Burkhardt, A. M., Long Kelvin Lee, K., Bryan Changala, P., et al. 2021, *ApJL*, **913**, L18
 Carty, D., Le Page, V., Sims, I. R., & Smith, I. W. M. 2001, *CPL*, **344**, 310
 Cernicharo, J., Agúndez, M., Cabezas, C., et al. 2021a, *A&A*, **649**, L15
 Cernicharo, J., Agúndez, M., Kaiser, R. I., et al. 2021b, *A&A*, **652**, L9
 Cheikh Sid Ely, S., Morales, S. B., Guillemin, J.-C., Klippenstein, S. J., & Sims, I. R. 2013, *JPCA*, **117**, 12155
 Cooke, I. R., Gupta, D., Messinger, J. P., & Sims, I. R. 2020, *ApJL*, **891**, L41
 Dobashi, K., Shimoikura, T., Nakamura, F., et al. 2018, *ApJ*, **864**, 82
 Dobashi, K., Shimoikura, T., Ochiai, T., et al. 2019, *ApJ*, **879**, 88
 Doddipatla, S., Galimova, G. R., Wei, H., et al. 2021, *SciA*, **7**, eabd4044
 Frisch, M. J., Trucks, G. W., Schlegel, H. B., et al. 2016, Gaussian16
 Revision C.01
 Georgievskii, Y., & Klippenstein, S. J. 2007, *JPCA*, **111**, 3802
 Grabow, J.-U., Palmer, E. S., McCarthy, M. C., & Thaddeus, P. 2005, *RSci*, **76**, 093106
 Gratier, P., Majumdar, L., Ohishi, M., et al. 2016, *ApJS*, **225**, 25
 Huang, C. H., Kaiser, R. I., & Chang, A. H. H. 2009, *JPCA*, **113**, 12675
 Landera, A., & Mebel, A. M. 2013, *JChS*, **135**, 7251
 Lee, K. L. K., Loomis, R. A., Xue, C., El-Abd, S., & McGuire, B. A. 2021a, *molsim*, Zenodo, doi:10.5281/ZENODO.5497790
 Lee, K. L. K., Changala, P. B., Loomis, R. A., et al. 2021b, *ApJL*, **910**, L2
 Lee, K. L. K., & McCarthy, M. 2020, *JPCA*, **124**, 898
 Lee, K. L. K., McGuire, B. A., & McCarthy, M. C. 2019, *PCCP*, **21**, 2946
 Lee, K. L. K., Loomis, R. A., Burkhardt, A. M., et al. 2021c, *ApJL*, **908**, L11
 Loomis, R. A., Burkhardt, A. M., Shingledecker, C. N., et al. 2021, *NatAs*, **5**, 188
 McCarthy, M. C., Lee, K. L. K., Loomis, R. A., et al. 2021, *NatAs*, **5**, 176
 McCarthy, M. C., & McGuire, B. A. 2021, *JPCA*, **125**, 3231
 McGuire, B. A., Burkhardt, A. M., Kalenskii, S., et al. 2018, *Sci*, **359**, 202
 McGuire, B. A., Burkhardt, A. M., Loomis, R. A., et al. 2020, *ApJL*, **900**, L10
 McGuire, B. A., Loomis, R. A., Burkhardt, A. M., et al. 2021, *Sci*, **371**, 1265
 Messinger, J. P., Gupta, D., Cooke, I. R., Okumura, M., & Sims, I. R. 2020, *JPCA*, **124**, 7950
 Siebert, M. A., Lee, K. L. K., Remijan, A. J., et al. 2022, *ApJ*, **924**, 21
 Sims, I. R., Queffelec, J.-L., Travers, D., et al. 1993, *CPL*, **211**, 461
 Tielens, A. G. G. M. 2008, *ARA&A*, **46**, 289
 Turner, B. E. 1991, *ApJS*, **76**, 617
 Woon, D. E. 2006, *CP*, **331**, 67
 Woon, D. E., & Herbst, E. 1997, *ApJ*, **477**, 204
 Xue, C., Willis, E. R., Loomis, R. A., et al. 2020, *ApJ*, **900**, L9